Results in Physics 53 (2023) 106975

Contents lists available at ScienceDirect

Results in Physics

journal homepage: www.elsevier.com/locate/rinp

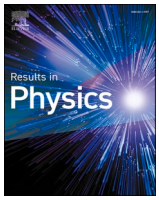

Electrospun PVDF/Barium hexaferrite fiber composites for enhanced electromagnetic shielding in the X-band range

M.M. Salem [a], El-Refaie Kenawy [b], Hesham M.H. Zakaly [c,d,e,*], Antoaneta Ene [f,*], Mohamed M. Azaam [b], Tarek B. Edries [g], Di Zhou [h], Marwa M. Hussein [a], Anwer S. Abd El-Hameed [i], Islam M. Nabil [j], Moustafa A. Darwish [a]

[a] Physics Department, Faculty of Science, Tanta University, Tanta 31527, Egypt
[b] Polymer Research Group, Chemistry Department, Faculty of Science, Tanta University, Tanta 31527, Egypt
[c] Physics Department, Faculty of Science, Al-Azhar University, Assiut Branch, Egypt
[d] Istinye University, Faculty of Engineering and Natural Sciences, Computer Engineering Department, Istanbul 34396, Turkey
[e] Institute of Physics and Technology, Ural Federal University, Yekaterinburg 620002, Russia
[f] Department of Chemistry, Physics and Environment, INPOLDE Research Center, Dunarea de Jos University of Galati, 47 Domneasca Street, 800008 Galati, Romania
[g] Cotton Pesticides Evaluation Department, Plant Protection Research Institute, Agricultural Research Centre, Giza, Egypt
[h] Electronic Materials Research Laboratory, Key Laboratory of the Ministry of Education &International Center for Dielectric Research, School of Electronic Science and Engineering, Xi'an Jiaotong University, Xi'an 710049, China
[i] Electronics Research Institute, Giza 12622, Egypt
[j] Physics Department, Faculty of Science, Fayoum University, Fayoum, Egypt

ARTICLE INFO

Keywords:
Electromagnetic shielding
Fiber composite
Polyvinylidene fluoride
Barium hexaferrite
Reflection loss

ABSTRACT

In the contemporary, digitally–driven era, the prevalence of electronic devices has drastically escalated electromagnetic (EM) pollution levels, marking a significant environmental challenge. Electrospun fiber composites of polyvinylidene fluoride (PVDF) and Barium hexaferrite (BHF) were analyzed for their potential usage in X-band electromagnetic shielding applications (EMSAs). Pure PVDF and BHF-PVDF fiber composite were manufactured by needleless electrospinning. X-ray diffraction (XRD), Fourier-transform infrared spectroscopy (FTIR), scanning electron microscopy (SEM), thermogravimetric analysis (TGA), vibrating sample magnetometer (VSM), and EM measurements utilizing a vector network analyzer (VNA) are all used to describe the prepared samples. The XRD and FTIR analyses confirmed the successful incorporation of BHF into the PVDF matrix. The results show that adding PVDF to BHF in fiber form enhances the reflection loss (RL), indicating improved electromagnetic shielding effectiveness (EMSE). The SEM analysis revealed that the fiber composite had a uniform fiber diameter distribution. In contrast, the TGA analysis demonstrated good thermal stability of the fiber composite. Polymer samples were evaluated to enhance gamma radiation and neutron particle attenuation. MCNP5 and Phy-X/PSD software were used to study semi-crystalline fluorocarbon polymer (PVDF) and barium hex ferrite BaFe12O19 (30 wt%) with PVDF (70 wt%). The MCNP5 programme simulated 0.015–15 MeV radiation attenuation. Additionally, the Phy-X/PSD programme verified the simulated μ values for the chosen Mxenes materials. The MCNP-5 code and Phy-X/PSD results were agreed. The linear attenuation coefficients for the polymer samples ranged from 3.166 to 0.032 $cm^2.g^{-1}$ for PVDF and from 73.960 to 0.113 $cm^2.g^{-1}$ for PVDF and BHF-PVDF Fiber at photon energies from 0.015 to 15 MeV. Overall, the electrospun fiber composite of PVDF and BHF particles shows promise for EMSAs in the X-band range. The enhanced RL observed in our study suggests that these fiber composites could be used to protect against electromagnetic radiation (EMR) from electronic devices, which is increasingly concerning in today's modern society.

* Corresponding authors.
E-mail addresses: h.m.zakaly@gmail.com, h.m.zakaly@azhar.edu.eg (H.M.H. Zakaly), Antoaneta.Ene@ugal.ro (A. Ene).

https://doi.org/10.1016/j.rinp.2023.106975
Received 3 July 2023; Received in revised form 30 August 2023; Accepted 10 September 2023
Available online 18 September 2023

Introduction

In contemporary society, the ubiquity of electronic apparatuses has precipitated a pronounced escalation in electromagnetic (EM) interference. This phenomenon has recently been underscored as a paramount issue of academic and practical interest [1–6]. In the realm of material science, it is salient to note that diverse two/ three-dimensional (2D/3D) architectures, such as graphene, MXene, and conductive polymers, have been judiciously employed to enhance the microwave absorption properties [5,7–9].

The X-band microwave frequency spectrum, spanning from 8.2 GHz to 12.4 GHz, holds significant import. This range is prevalently engaged in pivotal endeavors encompassing radio transmissions, RADAR systems, satellite operations, and extraterrestrial communication modalities [10]. Subjecting living entities, inclusive of humans, to electromagnetic radiation (EMR) within this frequency spectrum may precipitate detrimental biological consequences [4,11]. Consequently, an amplifying imperative exists for developing efficacious shielding substrates tailored to mitigate EMR spanning from 8.2 GHz to 12.4 GHz. Composites based on PVDF [12–15] and spinel/*hexa*-ferrites [16] or have shown promise in effectively shielding against EMR. PVDF, being a polar polymer [17], lends itself to transformation into fibers via electrospinning [18–20], making it a superior candidate for composite creation. Its unique electroactive phases make PVDF suitable for EMR shielding applications [17].

Meanwhile, BHF, known for its distinctive magnetic properties and high Curie temperature, is ideal for formulating composites with high magnetic loss factors [21–26]. When combined within a polymer matrix, the resultant composite inherits magnetic and dielectric properties, optimally positioning it for effective EMR shielding [27–32]. Apart from their EM shielding capabilities, the unique characteristics of fibers have unlocked a wide array of opportunities across various technological applications. For instance, fibers can enhance antennas' mechanical strength and facilitate antenna structure formation with high aspect ratios and anisotropic properties [33–35].

The effectiveness of these composites is critically dependent on the fabrication procedure. Needle electrospinning is a technique that eliminates the use of a needle or wire and subjects a polymer solution to a high electric field [18,19,36]. This procedure results in fibers with diameters ranging from tens to hundreds of nanometers. The ability to create aligned fibers further escalates the anisotropic properties of the composite material [20,37]. Despite the demonstrated potential of PVDF–BHF composites and fiber composites for efficient EMR shielding within the X-band frequency range, efforts to refine these materials and their manufacturing methods continue. Such investigations aim to augment shielding efficiency against EMR across an extensive frequency range [38–40].

According to the literature [41], the authors prepared BHF/PVDF nanocomposite films for energy storage applications. It's observed that the beta phase begins to diminish concurrently with an augmentation in the alpha phase, leading to a metamorphosis in the crystallinity of the nanocomposite when the BHF increases by more than 30%. Notably, the nanocomposite's dielectric constant achieves its zenith at a 30% BHF concentration. Still, any increment beyond this concentration instigates a decline. Furthermore, post the threshold of 30% BHF, and there's a stark escalation in the nanocomposite's leakage current density, signifying a heightened conductive trajectory stemming from inter-particle interactions. The dimension of the core–shell architecture, a product of PVDF and BHF nanoparticles, inversely correlates with the BHF concentration in the nanocomposite. To encapsulate, surpassing the 30% BHF concentration heralds a transformation in the PVDF-BHF nanocomposite's attributes, encompassing its crystalline nature, dielectric constant, leakage current density, and particulate dimensions. So, 30% BHF was used in our study.

This study delves into the impacts of fabricating BHF–PVDF composite fiber using a needleless electrospinning technique on its EM properties. Focusing specifically on its implications for EM shielding, we offer fresh insights into developing and optimizing these composite materials for mitigating EM pollution.

Materials and methods

Commercial PVDF (average molecular weight ~ 534000 by GPC powder) was purchased from Sigma-Aldrich. The conventional solid-state reaction method obtained barium hexaferrite $BaFe_{12}O_{19}$ (BHF). The desired stoichiometry was achieved by mixing powder containing high-purity Fe_2O_3 (Sigma-Aldrich, molecular weight = 159.69, purity ≥ 96%) and $BaCO_3$ (Sigma-Aldrich, molecular weight = 197.34, purity ≥ 99%) [42,43]. Following their formation, the mixtures of oxides and carbonates underwent homogenization and mechanical activation through ball milling for 4 h at a rotational speed of 1000 revolutions per minute. After applying a 10 Ton press to the sample, it underwent a sintering process in an air environment for 4 h at a temperature of 1200 °C. After the synthesis, the specimen underwent a gradual cooling process at 100 °C per hour and was subjected to dry milling. After acquiring the powder, it underwent a secondary compression. It was subjected to sintering at 1100 °C for 4 h in an ambient atmosphere. After the second sintering, the sample was ground again using agate mortal and ball milling to obtain fine powder for the characterizations and prepare 30 wt% BHF/70 wt% PVDF composite fiber by needleless electrospinning technique (made in China by Qingzi Nano model E03–001). The exact process was also used for preparing the pure PVDF fiber. To determine what elements were present in the produced samples, an Empyrean Panalytical diffractometer was used to run XRD analysis at room temperature ($10^\circ \leq 2\theta \geq 80^\circ$, Cu-$K_\alpha$, =1.54 Å). An FTIR spectrometer from the JASCO FT/IR4100 series was used to analyze the samples' composition from 4000 to 400 cm^{-1}. Zeiss (EVO-10) scanning electron microscopes were used to examine the surface microstructure of all synthetic samples. TGA was conducted utilizing a Perkin Elmer TGA–4000 thermogravimetric analyzer (United States). Alumina crucibles contained 7.2 mg of PVDF fiber and 13.4 mg of BHF–PVDF fiber. The samples were subjected to a temperature scan from 50 to 800 °C at 30 °C/min under a nitrogen atmosphere with a 20 ml/min flow rate. The magnetic characteristics of the produced samples were measured at room temperature using a Lake Shore model 7410-VSM and a magnetic field of up to 2 T. The following dimensions were used to compress the produced fibers: 22.86 × 10.16 × 2 mm^3. The X-band EM shielding properties of the produced samples were investigated using a Rohde & Schwarz (ZVA67-VNA) equipped underwent full 2–port calibration with a rectangular waveguide WR-90 to measure electrical and magnetic parameters (photo of the used setup is provided in the supplementary file (Fig. S1)). The real and imaginary components of the permittivity (ε) and permeability (μ) were computed using the Nicolson-Ross-Weir method, with the transmission/reflection line technique and the observed S-parameters. The expression of microwave absorption in the prepared samples, which protects against electromagnetic interference (EMI), is denoted by the reflection loss (*RL*). The *RL*, expressed in decibels (dB), was determined for all prepared samples using the following equation [44,45]:

$$RL(dB) = 20\log\left|\frac{(Z_{in}/Z_o)-1}{(Z_{in}/Z_o)+1}\right| \quad (1)$$

where Z_{in} and Z_o are the input impedance of EMI shielding material and the impedance of free space, respectively. The following equation can calculate the input impedance (Z_{in}/ Z_o):

$$Z_{in}/Z_o = \sqrt{\frac{\mu_r}{\varepsilon_r}}\left(\tanh\left[j\frac{2\pi fd}{c}\sqrt{\mu_r\varepsilon_r}\right]\right) \quad (2)$$

where ε_r and μ_r are the complex permittivity and permeability of the material used as the absorber shield, respectively, and d is the prepared samples' thickness (~2 mm). *c* is the velocity of light in air.

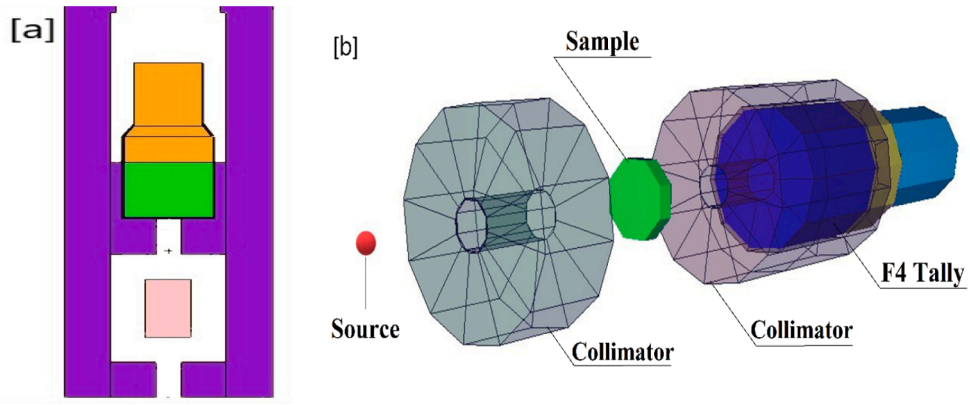

Fig. 1. (a,b): (a) 2D view and (b) 3D dynamic view of the used radiation attenuation simulation system for the [XPbO:(45-X)B_2O_3] polymer samples.

MCNP simulation

Monte-Carlo for nature particles code MCNP5 (MC) was used to simulate the irradiation of the examined polymer samples with a mono-energetic point source in the energy range of 0.015——15 MeV. It promotes the flow of electrons, neutrons, and gamma rays while taking into account the laws of physics interaction (photo-electric (PEE), Compton scattering (CSE), and pair formation processes (PPE))[46,47]. As seen in Fig. 1(a,b), MC input files need precise data (e.g., source dimensions, source-to-detector distance, geometry, elemental chemical composition, etc.)**. X(a,b).,** All parameters have been taken into account by the experimental system. MC input files were created in text format[46,48]. The cell described six components: radioactive source, primary (gamma rays' collimator, cubic sample, secondary (-rays collimator, and detector for both components in a Text format file. The radioactive source was positioned inside the back of a lead collimator of the primary γ-rays with a 0.14 cm radius and 0.3 cm height and positioned 15 cm away from the detector. A γ-rays point source was identified as an SDEF mono-energetic beam for each input file in the 0.015 – 15 MeV energy range. A neutron source was described as a californium watt fission spectrum in the energy range of 1–12 MeV for fast removal cross-section attenuation. The samples were created as a cubic layer positioned in the distance between the source and the detector. In addition, the elemental composition and densities of the studied samples were created in the material card of the text file. The detector was configured inside a lead collimator of the secondary γ-rays. The command tallies F4:P, and F4:N determines the average track length of the incident γ-rays and neutrons emitted from simulated gamma and neutron sources. An outer lead shield surrounded the created (detector, source, collimators, and samples). All the calculations are carried out on a core i5–2.3 GHz processor with several histories of NPS (107(for each file to achieve random statistical errors of better than (1 %).

Phy-X/PSD software

The Phy-X/PSD software (PhX) is an online program that computes numerous variables related to the shielding and attenuation for the studied material compositions, dosimetry[49,50]. Many calculations

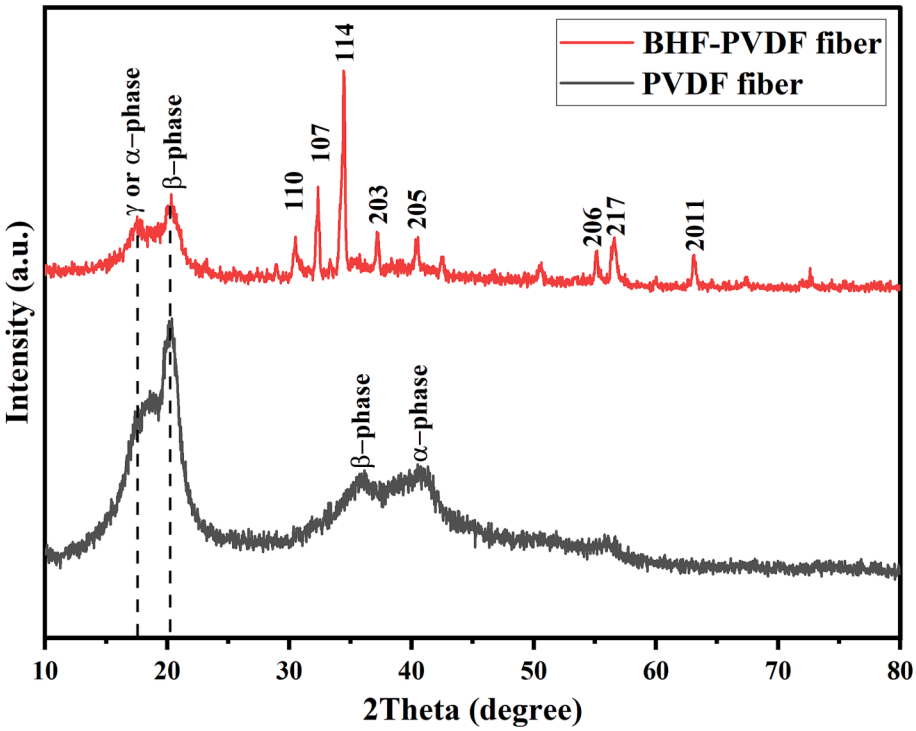

Fig. 2. XRD characteristics of PVDF fiber and BHF–PVDF composite fiber.

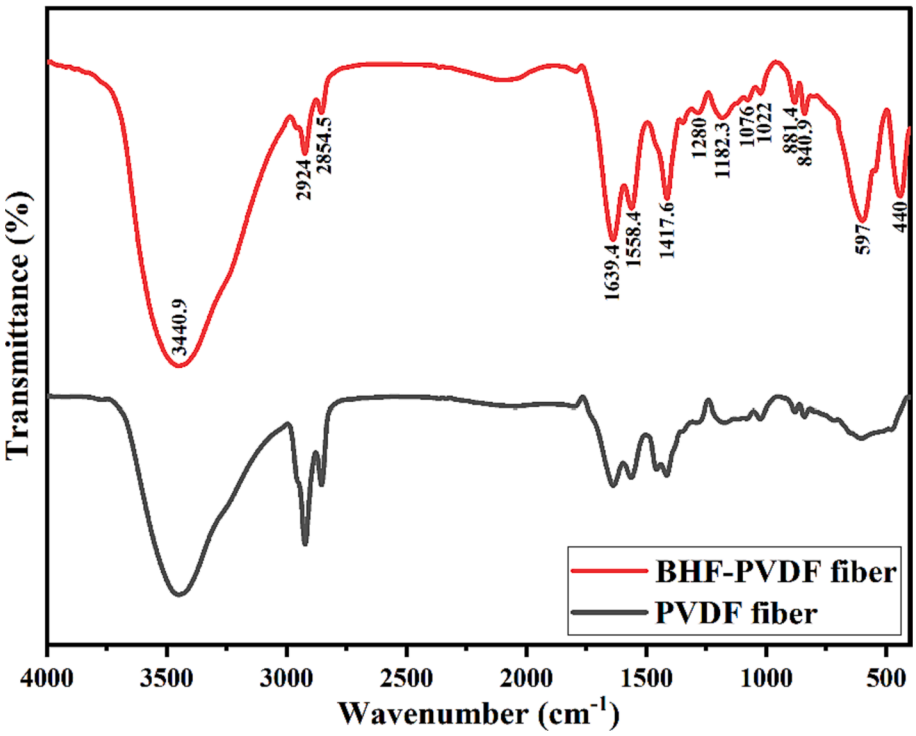

Fig. 3. FTIR spectra of PVDF fiber and BHF–PVDF composite fiber.

were performed using the PhX input file, including those for the linear attenuation coefficients (μ), the mass attenuation coefficients (μ_m), [51,52]. Also, the obtained results from PhX were used to be compared with the results obtained from MC to calculate the relative differences (Diff., %) as follows[53,54]:

$$Diff.(\%)|\frac{MCNP5 - Phy - X}{MCNP5}| \times 100 \quad (1)$$

Results and discussions

XRD discussion

The composite material has been verified to contain both PVDF and BHF phases through XRD analysis, as shown in Fig. 2. The confirmation of BHF phase formation with space group (P63/mmc) in all samples under investigation was established through reference to the BHF database (ICDD cards no. 00–027–1029 and 00–007–0276) [55,56]. The primary peaks of BHF are observed at (110), (107), (114), (203), (205), (206), (217), and (2011), with corresponding 2θ (2Theta) values of approximately 30.5°, 32°, 34°, 37°, 40°, 55°, 56°, and 63°, respectively. The potential of PVDF is becoming increasingly attractive due to the high electrical activity of both β and γ–phases [55]. However, it is noteworthy that solely γ and α exhibit additional peaks at approximately 17.7°, as depicted in the BHF–PVDF fiber specimen, rendering them readily distinguishable from the β–phase. The β–phase exhibits a distinct peak at approximately 2θ≈ 20°, as evidenced by the two prepared samples. The XRD outcomes may cause ambiguity distinguishing between the α and γ–phases. At the same time, the FTIR findings (which will be elaborated on subsequently) can differentiate between the α and γ–phases. Consequently, the simultaneous utilization of both methodologies would enable a precise differentiation among the primary stages (the exact phases) of PVDF [29,30,55]. The PVDF fiber specimen exhibited additional β and α–phases at 36° and 40°, respectively. These phases were not observed in the BHF–PVDF fiber specimen. This occurrence can be attributed to the prevalence and existence of high–intensity peaks originating from BHF [57,58]. Also, we can conclude from the XRD results that the β–phase is the most dominant phase in the prepared samples, and as evidenced by prior research [59–61], PVDF fibers fabricated through the electrospinning methodology exhibit a preference for the β–phase, attributed to the significant mechanical elongation and high electrical field inherent in this procedure. It is worth mentioning that XRD analysis of the pure BHF powder is provided in the supplementary file (Fig. S2).

FTIR discussion

Fig. 3 displays the FTIR transmission spectra of the prepared samples, covering the range from 4000 to 400 cm^{-1}. The spectral feature observed at approximately 3440 cm^{-1} is attributed to the vibrational mode associated with stretching O–H bonds in water molecules that are adsorbed onto the surface of PVDF [62]. The spectral peaks observed at 2924 and 2854 cm^{-1} are ascribed to the symmetric and asymmetric stretching vibrations of PVDF's carbon–hydrogen (C–H) bonds [62]. The 1417 and 1076 cm^{-1} spectral peaks correlate with the CH_2 wagging deformation [63]. The spectral peaks detected at 1417 and 1182 cm^{-1} correspond to the $–CF_2–$ and –C–F–functional groups, respectively [57]. The spectral samples exhibiting bands at approximately 1417, 1280, and 840 cm^{-1} indicate the β–crystalline phases. The bands observed around 1182, 881, and 840 cm^{-1} are attributed to the γ–phase, as previously reported in the literature [17,64]. The findings validate the presence of γ and β–phases in the prepared samples, and the β–phase is more dominant, as shown in the XRD results. The potential utility of the β–phase in EMSAs has been attributed to the non–zero dipole moment in the polymer chain [4]. The peaks observed at 597 and 440 cm^{-1} indicate the metal–oxygen stretching vibration of BHF, as reported in the literature [65]. And based on the absorbance values obtained from the FTIR measurements, the proportion of the β-phase among the crystalline region (F_β) can be quantitatively calculated using the equation presented by Gregorio & Cestari [41,66]. F_β is found to be 43.51% and 43.67 for PVDF fiber and BHF-PVDF fiber, respectively. From the results of F_β, it seems that the β-phase fraction content remains almost constant in PVDF and BHF-PVDF fiber. The inclusion of BHF has no impact on the β-phase

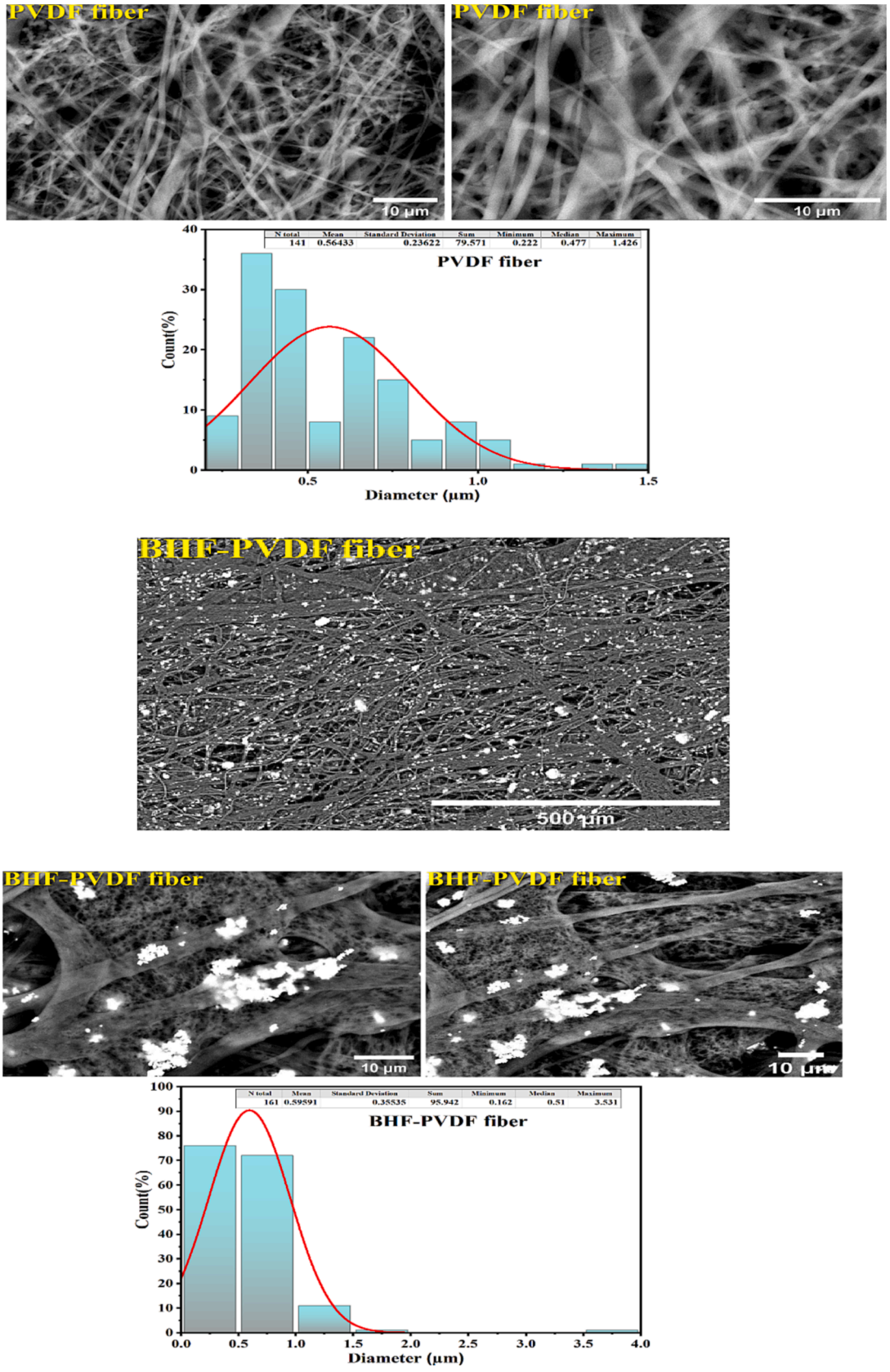

Fig. 4. SEM and average fibers diameter of PVDF fiber and BHF–PVDF composite fiber.

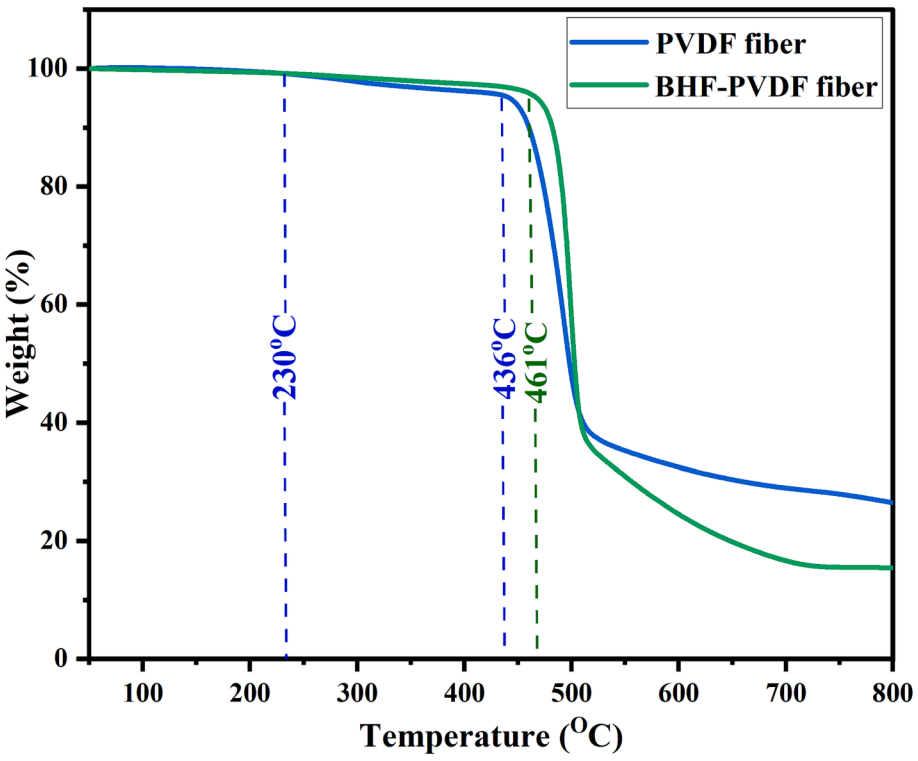

Fig. 5. TGA analysis of PVDF fiber and BHF–PVDF composite fiber.

fraction, which can be attributed to the higher concentration of PVDF (70 wt%) compared to BHF (30 wt%). Therefore there is no ionic interaction between the PVDF and the BHF to produce a β-phase of PVDF.

SEM discussion

Fig. 4 provides the SEM images of both PVDF fibers and the BHF–PVDF composite fibers. The images successfully showcase the results of the needles–based electrospinning technique used to fabricate

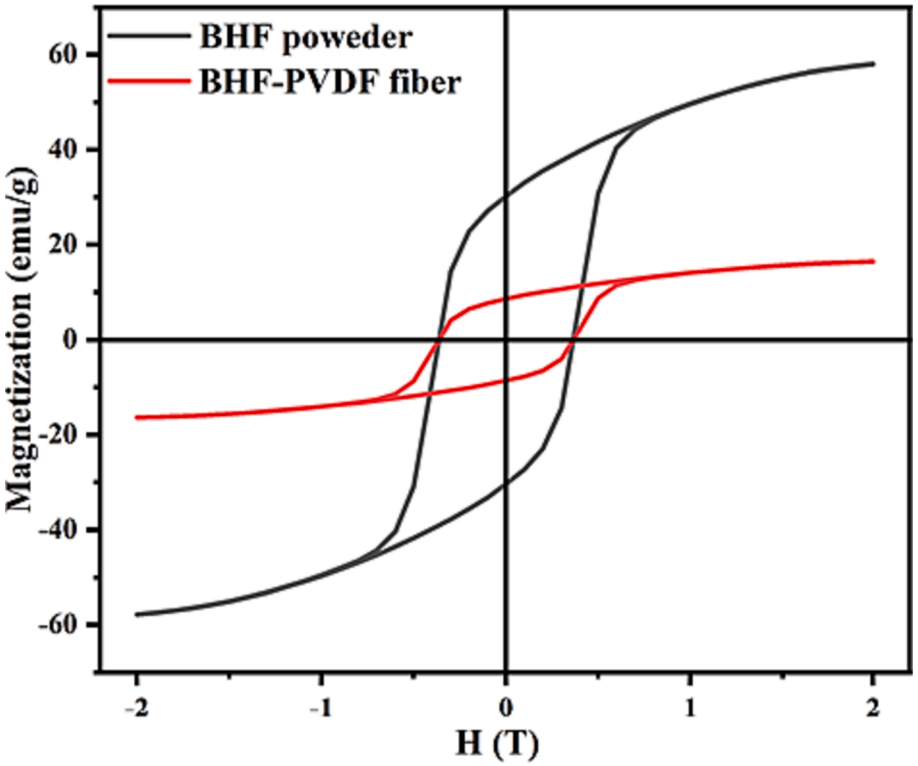

Fig. 6. VSM results of PVDF fiber and BHF–PVDF composite fiber.

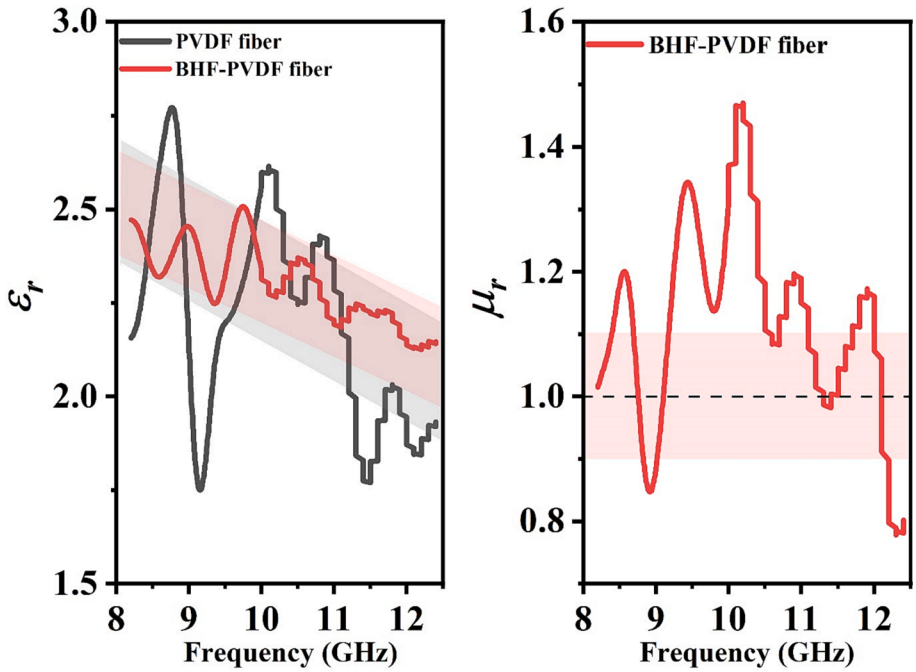

Fig. 7. Real part of permittivity and permeability of PVDF fiber and BHF–PVDF composite fiber.

these fibers. The technique has created fine, uniform fibers with the BHF particles evenly dispersed throughout the PVDF matrix, crucial for achieving the targeted magnetic properties. The PVDF fibers have an average diameter of approximately 0.56 μm. In contrast, the composite fibers show a slightly increased diameter, averaging 0.59 μm. This 6% increase in diameter can be attributed to integrating the BHF particles into the PVDF fibers, marking the successful creation of a composite material.

Furthermore, the SEM images demonstrate the encapsulation of BHF particles within the PVDF matrix. The effective embedding of BHF particles, a ferromagnetic material, within the PVDF fibers is expected to significantly impact the composite's magnetic properties. As revealed in the SEM images, the uniform dispersion of these particles implies an even distribution of magnetic properties throughout the composite material, ensuring its consistent performance under a magnetic field [19,67]. Thus, these SEM findings confirm the successful synthesis of BHF–PVDF composite fibers and provide essential insights into the material's morphology and potential magnetic behavior.

TGA discussion

The TGA was conducted to assess the thermal stability of the prepared samples. The TGA curves of the PVDF fiber and BHF–PVDF fiber are shown in Fig. 5. The PVDF fiber was subjected to two steps of degradation, the first at 230 °C to lose 5% of weight and the second at 436.4 °C to lose 60% of weight, leaving a residual of 26.9% at 800 °C. The BHF–PVDF fiber deterioration began at 461 °C and reached a weight loss of 62% at 515 °C. The TGA results demonstrate that the creation of PVDF fiber, which is boosted again by the inclusion of BHF, increases the thermal stability of PVDF fiber [68]. It is worth mentioning that the TGA analysis of the pure BHF and PVDF powders is provided in the supplementary file (Fig. S3).

VSM discussion

Fig. 6 shows how the BHF powder and the BHF–PVDF fiber behave differently when exposed to a magnetic field at room temperature. The BHF powder is a ferromagnetic material because it has a saturation magnetization (M_s) of 58 ± 0.5 emu/g and a coercivity (H_c) of 0.39 ± 0.02 T. This shows that an external magnetic field aligns the magnetic dipoles in the BHF particles and makes them less likely to become magnetized again.

Even though PVDF is not naturally magnetic, its hysteresis loops show that the BHF–PVDF composite has ferromagnetic properties. This event means that the BHF particles could cause magnetism in the PVDF matrix. The composite, on the other hand, has a lower saturation magnetization of 16 emu/g. This is likely because it has a nonmagnetic PVDF matrix and fewer magnetic BHF particles, which has a diluting effect. Still, the composite keeps the same coercivity value as the pure BHF particles. This shows that the BHF particles resist losing their magnetism, even when mixed with PVDF. BHF particles maintain their magnetic properties due to the inherent characteristics of BHF, like intrinsic magnetic nature, chemical stability, physical encapsulation, and high Curie temperature of BHF [21–26]. This is an excellent thing about the BHF–PVDF composite, making it even more likely to be used for EM shielding. Also, keeping a high H_c with decreasing M_s [69] when preparing composite fiber will lead to high anisotropy energy, enhancing the impedance matching and absorption of the studied sample [14,44].

EM properties discussion

In the realm of microwave absorbers, both permittivity and permeability play integral roles in determining material behavior. The permittivity can be chiefly attributed to conductive and relaxation losses, encompassing polarization and electron hopping phenomena. On the other hand, permeability reflects a material's magnetic response, often linked to magnetic dipoles and domain wall motion. The dipole and interfacial polarizations are of paramount significance, predominantly shaping the microwave attributes. The former stems from functional groups exhibiting disparities in electronegativity, while the latter originates at heterojunction interfaces.

Notably, imperfections, dislocations, and magnetic inhomogeneities augment the relaxation losses within these absorbers [70,71]. In Fig. 7, the real part of permittivity (ε_r) and permeability (μ_r) for both PVDF fiber and the BHF-PVDF composite fiber are presented in the frequency range from 8.2 to 12.4 GHz. The ε_r values for both materials are around 2.5, exhibiting a frequency dispersion of approximately 2. This

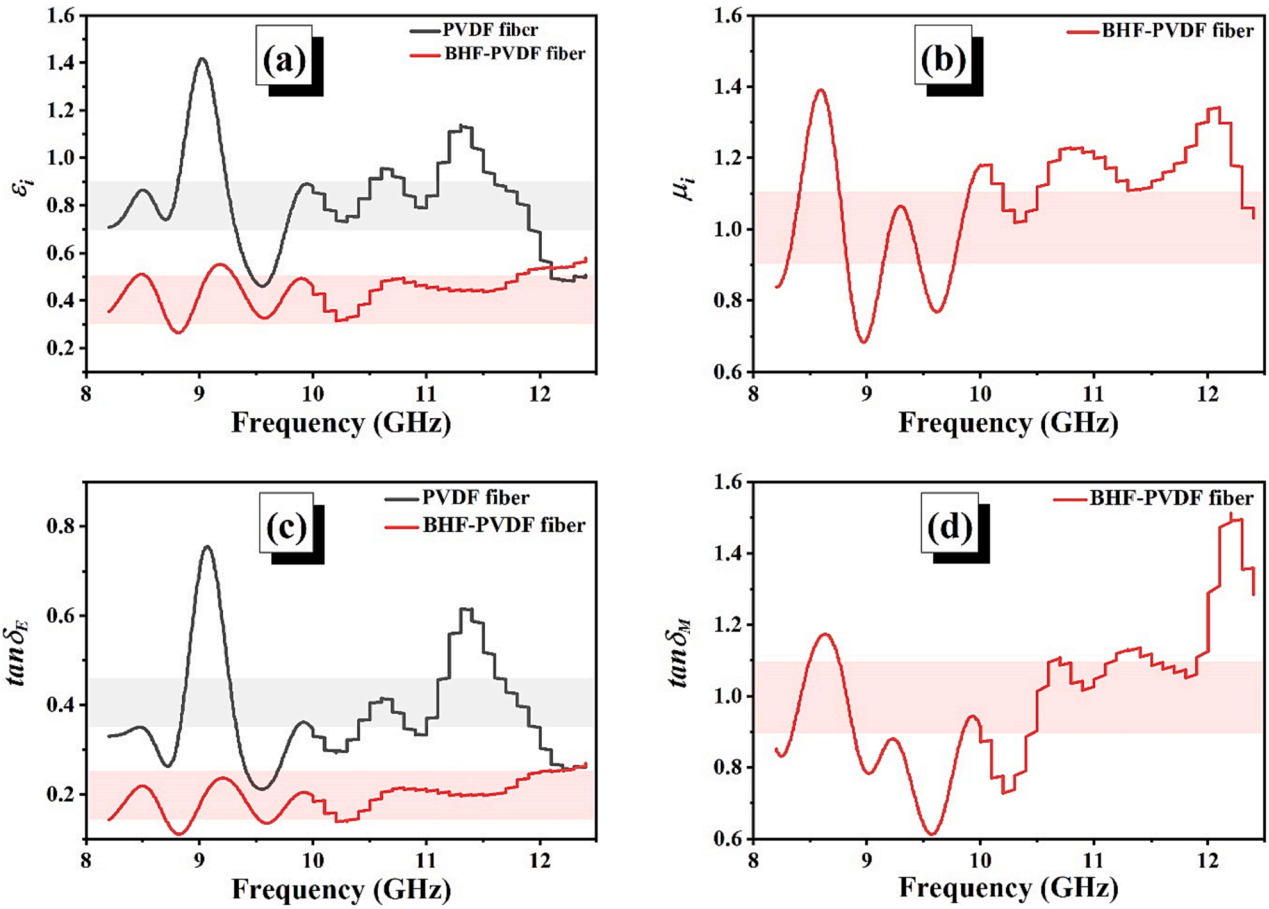

Fig. 8. Imaginary part of permittivity **(a)**, imaginary part of permeability **(b)**, dielectric loss **(c)**, and magnetic loss **(d)** of PVDF fiber and BHF–PVDF composite fiber.

dispersion suggests that the material's response to the electric field component of the EM wave changes across the frequency range. The dispersion might be caused by factors such as the composite material's interface polarization, the materials' inherent dielectric properties, and the distribution of BHF particles in the PVDF matrix [72–74].

Interestingly, despite PVDF's nonmagnetic nature, the BHF–PVDF composite fiber showcases a significant response to the electric field. This is likely due to the induction of magnetic properties in the PVDF matrix by the BHF particles. However, the μ_r for the BHF–PVDF composite fiber is around 1, affirming that PVDF does not exhibit magnetic properties. This value indicates that the magnetic field passes through the composite without substantial opposition, which is consistent with the nonmagnetic nature of the PVDF [75–77].

In this context, even though the composite's saturation magnetization is lower than that of pure BHF particles, its permittivity and permeability values align well with desired properties for EM shielding materials. The balance between permittivity and permeability underscores the composite's potential as an effective EM shield in the X-band frequency range.

Fig. 8 illustrates the imaginary part of permittivity (ε_i) and permeability (μ_i), as well as the dielectric ($tan\delta_E$) and magnetic ($tan\delta_M$) losses for PVDF and the BHF–PVDF composite fiber across the frequency range from 8.2 to12.4 GHz. The BHF–PVDF composite exhibits an ε_i of around 0.4, significantly less than the 0.8 observed for pure PVDF. This difference reflects the impact of BHF particles on the complex permittivity of the composite, potentially reducing the capacity of the material to polarize in response to an applied electric field [55,75–77].

On the other hand, the BHF–PVDF composite fiber shows a μ_i of approximately 1, suggesting a discernible magnetic response induced by the BHF particles. This response is pivotal in establishing the composite's interaction with the magnetic component of EM waves, ultimately contributing to its overall shielding effectiveness [14,44,78].

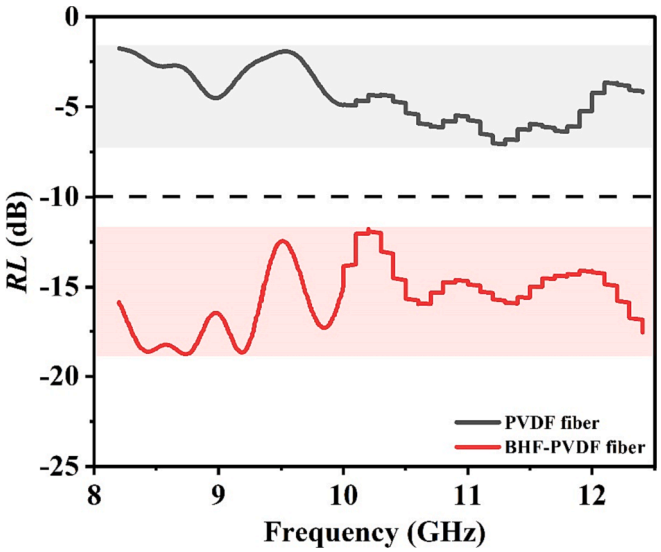

Fig. 9. Reflection loss (*RL*) of PVDF fiber and BHF–PVDF composite fiber.

Examining the $tan\delta_E$, the composite material's value is around 0.4, double that of the PVDF fiber, which is 0.2. This higher dielectric loss indicates a more significant potential for the BHF–PVDF composite to attenuate EM waves through electric dipole relaxation.

The $tan\delta_M$ for the composite is around 1, indicating that the

Table 1
The linear attenuation coefficient (μ) was obtained using MCNP5 and Phy-X for the polymer samples.

Energy, (MeV)	The linear attenuation coefficient (μ, cm^{-1})					
	PVDF Fiber			BHF-PVDF Fiber		
	MCNP5	Phy-X	Diff, (%)	MCNP5	Phy-X	Diff, (%)
0.015	3.166	3.193	0.832	73.960	74.364	0.546
0.03	0.651	0.665	2.175	11.215	11.292	0.686
0.05	0.367	0.378	2.759	5.391	5.444	0.994
0.08	0.292	0.298	1.999	1.999	2.036	1.829
0.1	0.270	0.276	1.925	1.394	1.424	2.168
0.2	0.216	0.220	1.697	0.712	0.729	2.378
0.3	0.188	0.190	1.333	0.573	0.583	1.893
0.4	0.169	0.170	0.975	0.503	0.509	1.355
0.5	0.154	0.155	0.837	0.455	0.460	1.011
0.6	0.142	0.144	0.818	0.420	0.423	0.825
0.8	0.125	0.126	0.538	0.368	0.370	0.464
1	0.112	0.113	1.391	0.327	0.332	1.331
2	0.079	0.079	0.566	0.231	0.233	0.675
3	0.063	0.064	0.529	0.189	0.190	0.618
4	0.055	0.055	0.351	0.165	0.166	0.498
5	0.049	0.049	0.284	0.150	0.151	0.404
6	0.045	0.045	0.364	0.140	0.141	0.445
8	0.040	0.040	0.180	0.128	0.128	0.355
10	0.036	0.036	0.171	0.121	0.121	0.264
15	0.032	0.032	0.102	0.113	0.113	0.158

BHF–PVDF composite fiber exhibits a robust magnetic relaxation. This, along with the observed dielectric loss, emphasizes the potential of the BHF–PVDF composite fiber for EMI shielding applications. The composite's notable performance in managing electric and magnetic interactions could play a key role in preventing the propagation of EM waves, thereby enhancing its shielding performance [55,75–77]. It's of significant scholarly interest to observe that both $tan\delta_E$ and $tan\delta_M$ manifest trends akin to those of ε_i [79] and μ_i, respectively.

The absorptive capability of a material is a testament to its proficiency in assimilating electromagnetic waves. Conventionally, a Reflection Loss (*RL*) value less than −10 dB signifies that the material can capture at least 90% of these waves. When these waves impinge upon the material's surface, a portion penetrates its core while the remainder is reflected. In our research endeavors, the extent to which these waves infiltrate the material's interior was quantified using impedance matching, as elucidated in Equations (1) and (2) [80,81]. Fig. 9 depicts the reflection loss (*RL*) for PVDF and BHF–PVDF composite fiber. The *RL* value emerges as a pivotal parameter in the discourse on materials suitable for EMSAs. Notably, diminished RL values indicate superior EM energy absorption and a consequential reduction in its reflection [79]. The *RL* of PVDF fiber is registered around −5 dB, suggesting a considerable reflection of incident EM waves. Contrastingly, the BHF–PVDF composite fiber showcases a much lower *RL*. This pronounced reduction indicates that the composite absorbs incident EM wave energy more, bolstering its shielding capabilities.

Moreover, it's noteworthy that literature sources affirm the superior

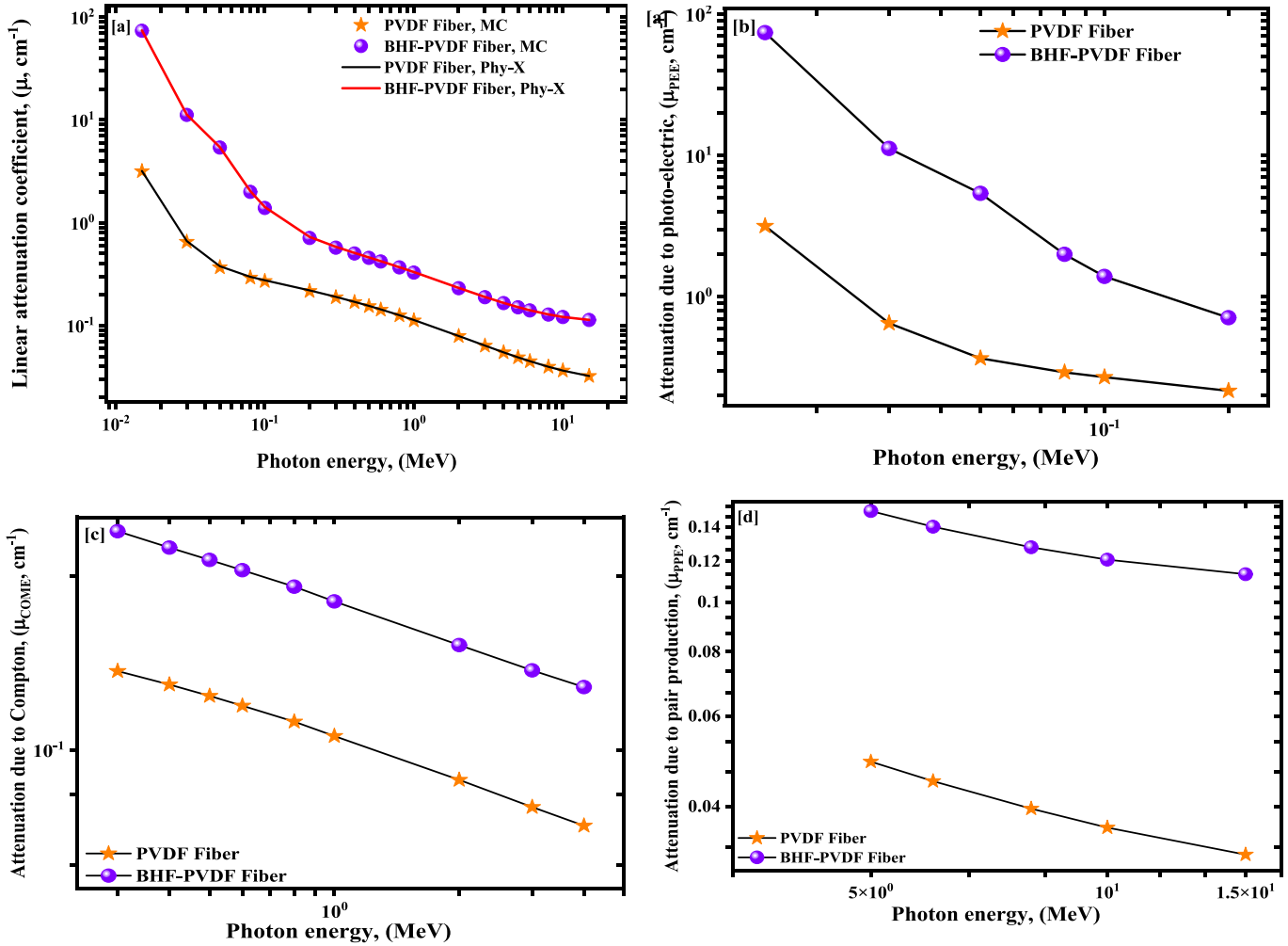

Fig. 10. (a-d) Influence of gamma-ray energy on linear attenuation coefficient obtained [a] From MC and Phy-X, and due to [b] Photo-electric,]c] Compton scattering, and [d] Pair production for the studied polymer samples vs. the photon energy.

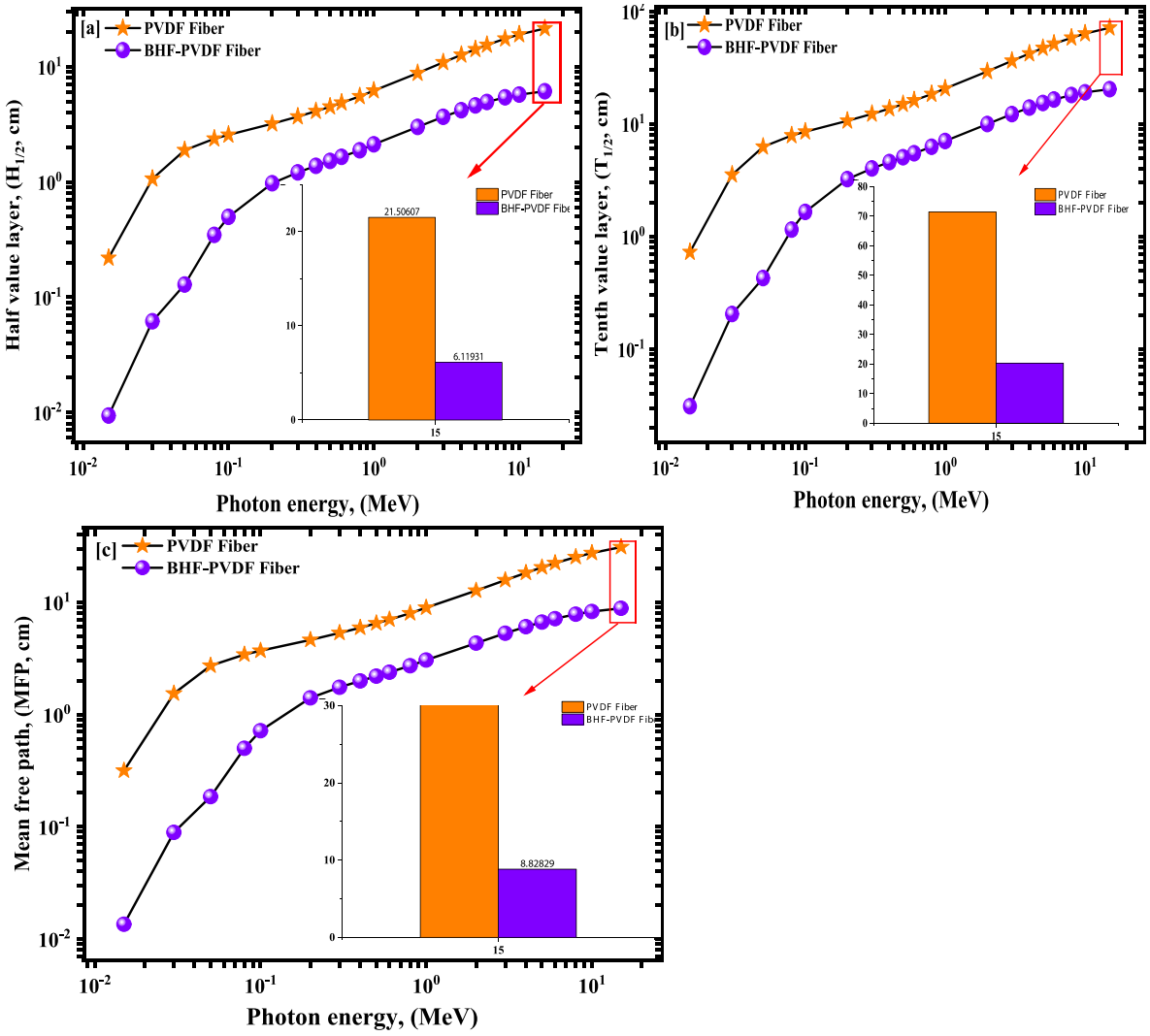

Fig. 11. (a-c) (a) The half value layer (HVL), (b) the tenth value layer (TVL), and (c) the mean free path (MFP) for the studied polymer samples vs. the photon energy.

RL performance of BHF–PVDF composite fiber compared to its fiber counterpart. This superiority can be ascribed to the inherent advantages of the fiber form, particularly the increased surface area that allows for more effective interactions with incident EM waves [44,78,82].

Interfacial polarization, a phenomenon occurring at the boundary between the PVDF matrix and the BHF particles, also plays a pivotal role in enhancing the *RL* of the composite fiber. This interfacial polarization disrupts the synchronization of the response to the incident EM waves, leading to an increase in energy absorption.

In essence, Fig. 9 provides compelling evidence of the promising potential of BHF–PVDF composite fiber for EMSAs, as manifested by its significantly reduced *RL*, the advantages associated with its fibrous form, and the notable contribution of interfacial polarization. It is worth mentioning that the *RL* of BHF–PVDF composite fiber at different thicknesses was simulated by the Matlab program provided in the supplementary file (Fig. S4).

Radiation shielding

The linear attenuation coefficient (μ) values for the two polymer samples (PVDF and BHF-PVDF Fiber) within the energy range of 0.015——15 MeV were assessed using MCNP5 code and Phy-X software to assess the radiation attenuation characteristics. The relative difference (Diff., %) between the results obtained from MCNP5 and Phy-X is listed in Table 1. The results showed good agreement with a maximum relative difference of 2.759 %. On the other hand, the linear attenuation coefficient (μ) of the two polymer samples decreases as the energy levels increase, a general trend observed across all materials. It is consistent with the behavior of radiation. This trend is particularly evident for the data where μ drops from 3.166 to 0.032 $cm^2.g^{-1}$ for the PVDF sample and from 73.960 to 0.113 $cm^2.g^{-1}$ for the PVDF and BHF-PVDF Fiber at photon energy range from 0.015 MeV to 15 MeV.

On the other hand, Fig. 10(a) represents that there is a strong reduction in the μ values for all prepared samples due to PEE interaction, which has cross-section changes with $E_\gamma^{-3.5}$. Therefore, the interaction cross-section reduced strongly with the enrichment of photon values, which is associated with a similar reduction in the photon-electron interactions and μ_L values. The enrichment of the applied E_γ values between 0.015 and 0.2 MeV causes a strong exponential decreasing trend from 3.166 to 0.216 $cm^2.g^{-1}$ for the PVDF sample and from 73.960 to 0.712 $cm^2.g^{-1}$ for the PVDF and BHF-PVDF Fiber. Furthermore, the enrichment of E_γ values above 0.2 MeV causes an exponential decrease in the μ values in the E_γ interval of 0.3 to 4 MeV, as presented in Fig. 10 (b). The exponential reduction is attributed to the CSE interaction with cross-section changes with E_γ^{-1}. This can be attributed to higher energy photons being less likely to interact with the atoms in the material due to their higher momentum[83]. Therefore, the probability of absorption

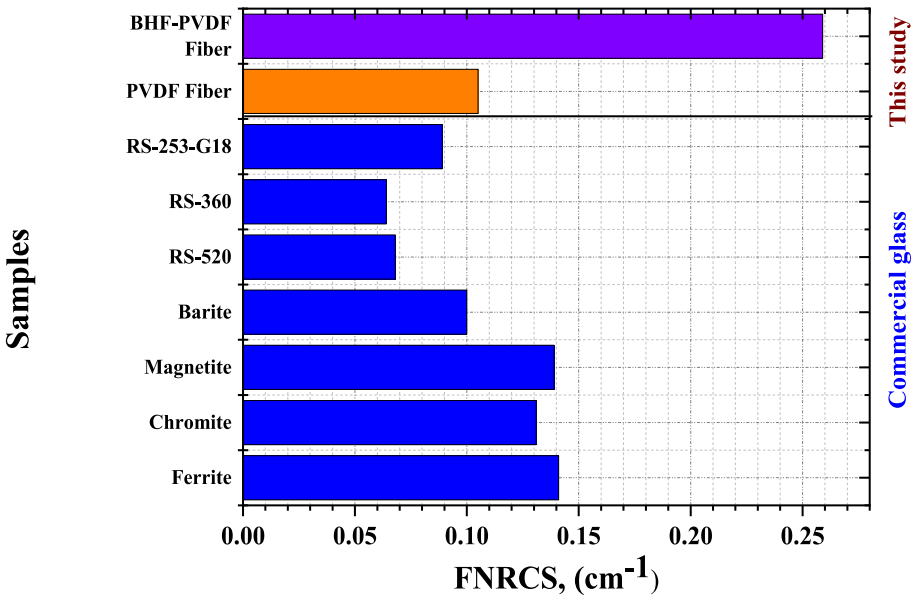

Fig. 12. Comparison of The fast neutron removal cross-section (FNRCS) obtained from MCNP5 for the studied samples and commercial glasses used for shielding/attenuation.

decreases associated with the increased probability of photons scattering with increasing energy. The enrichment in E_γ values was associated with a smooth decrease in the cross-section with decreases in the number of photon-electron interactions followed by a smooth reduction in the μ values. Fig. 10(b) depicts a reduction in the μ values from 0.188 to 0.055 $cm^2.g^{-1}$ for the PVDF sample and from 0.572 to 0.165 $cm^2.g^{-1}$ for the PVDF and BHF-PVDF Fiber with raising the E_γ values between 0.3 MeV and 4 MeV, respectively. Also, there is a little reduction due to the PPP interaction with cross-section changes with E_γ^2. The μ drops from 0.049 to 0.032 $cm^2.g^{-1}$ for PVDF sample and from 0.150 to 0.113 $cm^2.g^{-1}$ for the PVDF and BHF-PVDF Fiber with raising the E_γ values between 5 MeV and 15 MeV as seen in Fig. 10(c). The μ values for the BHF-PVDF Fiber are the highest among the other materials, indicating that it is the most effective polymer material for attenuating radiation.

Fig. 11(a) displays the fluctuation of the MFP vs. the photon energy for the chosen polymer samples. Based on the simulated μ values for a gamma-ray in the energy range of 0.015 – 15 MeV, the mean free path (MFP) of the examined materials was computed. Similar to the variance in μ values previously mentioned, the MFP values reflect an increasing trend, which varied from 0.316 to 31.027 $cm^2.g^{-1}$ for the PVDF sample and from 0.014 to 8.828 $cm^2.g^{-1}$ for the PVDF and BHF-PVDF Fiber. The BHF-PVDF Fiber may be better suited for radiation attenuation applications due to the lowest values of the MFP. The HVL (HVL $= \frac{\ln(2)}{\mu}$) and TVL (TVL $= \frac{\ln(10)}{\mu}$) are commonly used to measure the effectiveness of radiation shielding[84]. These checks can also be used to estimate the shielding material's thickness. Since radiation is attenuated as it travels through an increasingly small zone, radiation shielding efficacy improves with decreasing values of either parameter for a given photon energy. Typically, the HVL and TVL all go up and down in tandem. Fig. 11**(b,c)** presents the values of HVL and TVL. The HVL of the polymer samples increased as the values of μ decreased. Because of the opposite correlation between μ and HVL as well as TVL, the HVL values grew from 0.219 to 21.506 $cm^2.g^{-1}$ for the PVDF sample and from 0.009 to 6.119 $cm^2.g^{-1}$ for the PVDF and BHF-PVDF Fiber with raising the γ_e values from 0.015 MeV to 15 MeV, respectively as seen in Fig. 11b. The BHF-PVDF Fiber polymer sample has the lowest HVL values due to the high attenuation as well as the highest content of Ba and Fe. The fluctuations of TVL with photon energy are illustrated in Fig. 11c. The TVL values have the same trend as the HVL. The BHF-PVDF Fiber polymer sample has the lowest TVL values, indicating the high radiation shielding characteristics.

The probability that neutrons will pass through a substance without reacting is shown by the FNRCS ($\sum_R$). PVDF and BHF-PVDF samples have FNRCS values of 0.105 and 0.259, respectively. Also, FNRCS have been compared with other samples that contained chromite, ferrite, magnetite, and barite[85], commercial attenuation glasses RS-253-G18, RS-360, and RS-520, as represented in Fig. 12 [85,86]**.** That comparison showed that the BHF-PVDF sample has higher FNRCS values than those compared. Therefore, we may deduce that polymer samples have better neutron attenuation properties.

Conclusions

This study has successfully synthesized and characterized an electrospun fiber composite of PVDF and BHF, demonstrating their potential for efficient EMSAs. XRD and FTIR analyses confirmed the successful incorporation of BHF particles into the PVDF matrix and the dominant presence of the β–phase of PVDF, known for its contribution to EMSE. The SEM analysis revealed the composite's uniform fiber diameter distribution, indicating the effective electrospinning process. The magnetization loops further verified the ferromagnetic nature of the composite, with the BHF particles inducing ferromagnetism in the nonmagnetic PVDF matrix. Despite the composite's lower M_s compared to pure BHF, its H_c remained the same, showcasing its strong resistance to demagnetization. The composite's frequency–dependent permittivity and permeability showed notable dispersion, possibly due to interfacial polarization and PVDF's intrinsic nonmagnetic nature. The imaginary parts of permittivity and permeability, corresponding to dielectric and magnetic losses, also displayed unique characteristics. TGA results underscored the enhanced thermal stability of the composite, particularly with the inclusion of BHF, which commenced deterioration at higher temperatures compared to PVDF fiber alone. Lastly, regarding *RL*, the composite outperformed the pure PVDF fiber, particularly in the X-band range, further emphasizing its potential for EM shielding. The polymer samples PVDF and BHF–PVDF were assessed through the shielding qualities against gamma rays and neutrons of the synthesized polymer materials using the Monte Carlo simulation (MC) and Phy-X software in the gamma photon energy range of 0.015–15 MeV. Radiation shielding parameters, half value layer (HVL), tenth value layer

(TVL), mean free path (MFP) were calculated for the synthesized polymer samples. The μ values were varied from 3.166 to 0.032 $cm^2.g^{-1}$ for the PVDF sample and from 73.960 to 0.113 $cm^2.g^{-1}$ for the PVDF and BHF-PVDF Fiber at photon energy range from 0.015 MeV to 15 MeV. The BHF-PVDF Fiber polymer sample has the highest μ values and lowest HVL, TVL, and MFP values. Overall, this research offers valuable insights into the possibility of BHF–PVDF fiber composites in EMSAs, setting the stage for future studies to optimize these materials and broaden their applicability.

Declaration of Competing Interest

The authors declare that they have no known competing financial interests or personal relationships that could have appeared to influence the work reported in this paper.

Data availability

The datasets generated during and/or analyzed during the current study are available from the corresponding author on reasonable request.

Acknowledgment

Authors would like to acknowledge the financial support of this work by STDF, Egypt, through Project ID: 28971, Electrospun Organic Polymers for electronic devices applications. The author AE would like to thank the support of the research grant with contract no. 9187/2023, funded by Dunarea de Jos University of Galati, Romania.

Appendix A. Supplementary data

Supplementary data to this article can be found online at https://doi.org/10.1016/j.rinp.2023.106975.

References

[1] Zhang H, Cheng J, Wang H, Huang Z, Zheng Q, Zheng G, et al. Initiating VB-Group Laminated NbS2 Electromagnetic Wave Absorber toward Superior Absorption Bandwidth as Large as 6.48 GHz through Phase Engineering Modulation. Adv Funct Mater 2022;32. https://doi.org/10.1002/adfm.202108194.
[2] Wu Z, Cheng H-W, Jin C, Yang B, Xu C, Pei Ke, et al. Dimensional design and Core-Shell engineering of nanomaterials for electromagnetic wave absorption. Advanced Materials 2022;34(11). https://doi.org/10.1002/adma.202107538.
[3] Guan X, Yang Z, Zhu Y, Yang L, Zhou M, Wu Y, et al. the controllable porous structure and s-doping of hollow carbon sphere synergistically act on the microwave attenuation. Carbon N Y 2022;188:1–11.
[4] Chen G, Zhang L, Luo B, Wu H. Optimal control of the compositions, interfaces, and defects of hollow sulfide for electromagnetic wave absorption. Journal of Colloid and Interface Science 2022;607:24–33. https://doi.org/10.1016/j.jcis.2021.08.186.
[5] Peymanfar R, Yektaei M, Javanshir S, Selseleh-Zakerin E. Regulating the energy band-gap, UV–Vis light absorption, electrical conductivity, microwave absorption, and electromagnetic shielding effectiveness by modulating doping agent. Polymer (Guildf) 2020;209:122981. https://doi.org/10.1016/j.polymer.2020.122981.
[6] Peymanfar R, Javanshir S, Naimi-Jamal MR, Tavassoli SH. Morphology and medium influence on microwave characteristics of nanostructures: A review. Journal of Materials Science 2021;56:17457–77. https://doi.org/10.1007/s10853-021-06394-z.
[7] Peymanfar R, Selseleh-Zakerin E, Ahmadi A. Tailoring energy band gap and microwave absorbing features of graphite-like carbon nitride (g-C3N4). Journal of Alloys and Compounds 2021;867:159039. https://doi.org/10.1016/j.jallcom.2021.159039.
[8] Peymanfar R, Moradi F. Functionalized carbon microfibers (biomass-derived) ornamented by Bi2S3 nanoparticles: an investigation on their microwave, magnetic, and optical characteristics. Nanotechnology 2021;32:65201. https://doi.org/10.1088/1361-6528/abc2ec.
[9] Yuan H, Ma C, Gao Z, Zhang L. Preparation of NiCo 2 O 4 and NiCo 2 s 4 micro-onions for electrochemical sensing of glucose. Applied Physics A: Materials Science & Processing 2019;125. https://doi.org/10.1007/s00339-018-2363-1.
[10] Darwish KA, Hemeda OM, Abdel Ati MI, Abd El-Hameed AS, Zhou D, Darwish MA, et al. Synthesis, characterization, and electromagnetic properties of polypyrrole–barium hexaferrite composites for EMI shielding applications. Applied Physics A 2023;129:460. https://doi.org/10.1007/s00339-023-06738-3.
[11] Peymanfar R, Selseleh-Zakerin E, Ahmadi A, Tavassoli SH. Architecting functionalized carbon microtube/carrollite nanocomposite demonstrating significant microwave characteristics. Scientific Reports 2021;11:1–15. https://doi.org/10.1038/s41598-021-91370-5.
[12] Peymanfar R, Fazlalizadeh F. Microwave absorption performance of ZnAl2O4. Chemical Engineering Journal 2020;402:126089. https://doi.org/10.1016/j.cej.2020.126089.
[13] Peymanfar R, Ahmadi A, Selseleh-Zakerin E. Evaluation of the size and medium effects on the microwave absorbing, magnetic, electromagnetic shielding, and optical properties using CuCo2S4 nanoparticles. Journal of Alloys and Compounds 2020;848:156453. https://doi.org/10.1016/j.jallcom.2020.156453.
[14] Darwish MA, Morchenko AT, Abosheiasha HF, Kostishyn VG, Turchenko VA, Almessiere MA, et al. Impact of the exfoliated graphite on magnetic and microwave properties of the hexaferrite-based composites. Journal of Alloys and Compounds 2021;878:160397.
[15] Peymanfar R, Ghorbanian-Gezaforodi S, Selseleh-Zakerin E, Ahmadi A, Ghaffari A. Tailoring La0.8Sr0.2MnO3/La/Sr nanocomposite using a novel complementary method as well as dissecting its microwave, shielding, optical, and magnetic characteristics. Ceramics International 2020;46:20896–904. https://doi.org/10.1016/j.ceramint.2020.05.139.
[16] Peymanfar R, Javanshir S, Naimi-Jamal MR, Cheldavi A, Esmkhani M. Preparation and characterization of MWCNT/Zn 0.25 co 0.75 fe 2 O 4 nanocomposite and investigation of its microwave absorption properties at x-Band frequency using silicone rubber polymeric matrix. Journal of Electronic Materials 2019;48:3086–95. https://doi.org/10.1007/s11664-019-07065-1.
[17] Ruan L, Yao X, Chang Y, Zhou L, Qin G, Zhang X. Properties and applications of the β phase poly(vinylidene fluoride). Polymers (Basel) 2018;10(3):228.
[18] Blachowicz T, Ehrmann A. Most recent developments in electrospun magnetic nanofibers: A review. J Eng Fiber Fabr 2020;15. https://doi.org/10.1177/1558925019900843.
[19] Dorneanu PP, Cojocaru C, Olaru N, Samoila P, Airinei A, Sacarescu L. Electrospun PVDF fibers and a novel PVDF/CoFe2O4 fibrous composite as nanostructured sorbent materials for oil spill cleanup. Applied Surface Science 2017;424:389–96.
[20] Mahato B, Lomov S V, Shiverskii A, Owais M, Abaimov SG. A Review of Electrospun Nanofiber Interleaves for Interlaminar Toughening of Composite Laminates. Polymers (Basel) 2023;15. https://doi.org/10.3390/polym15061380.
[21] Yasmin N, Yasmin S, Zahid M, Gillani SF, Islam MU, Altaf M, et al. Impact of Ho-Ni substitution on structural, morphological and dielectrical characteristics of BaFe12O19 m-type hexagonal ferrite. Physica B: Condensed Matter 2020;581:411950.
[22] Kumar S, Prakash J, Verma A, Jasrotia R. A comprehensive review of synthesis, properties, and applications of BaFe12O19 hexaferrites. Materials Today: Proceedings 2023.
[23] Qiu J, Zhang Q, Gu M, Shen H. Effect of aluminum substitution on microwave absorption properties of barium hexaferrite. J Appl Phys 2005;98. https://doi.org/10.1063/1.2135412.
[24] Rhein F, Helbig T, Neu V, Krispin M, Gutfleisch O. in-situ magnetic force microscopy analysis of magnetization and demagnetization behavior in Al3+ substituted sr-hexaferrite. Acta Materialia 2018;146:85–96. https://doi.org/10.1016/j.actamat.2017.12.010.
[25] Salem MM, Panina LV, Trukhanova EL, Darwish MA, Morchenko AT, Zubar TI, et al. Structural, electric and magnetic properties of (BaFe11.9Al0.1O19)1–x -(BaTiO3)x composites. Composites Part B: Engineering 2019;174. https://doi.org/10.1016/j.compositesb.2019.107054.
[26] Darwish MA, Kostishyn VG, Korovushkin VV, Isaev IM, Morchenko AT, Panina LV, et al. Tuning the magnetic order in Sc-Substituted barium hexaferrites. IEEE Magnetics Letters 2019;10:1–5.
[27] Jurczuk K, Galeski A, Mackey M, Hiltner A, Baer E. Orientation of PVDF α and γ crystals in nanolayered films. Colloid & Polymer Science 2015;293:1289–97. https://doi.org/10.1007/s00396-015-3542-7.
[28] Martins P, Lopes AC, Lanceros-Mendez S. Electroactive phases of poly(vinylidene fluoride): Determination, processing and applications. Progress in Polymer Science 2014;39:683–706. https://doi.org/10.1016/j.progpolymsci.2013.07.006.
[29] Banerjee P, Bhattacharjee Y, Bose S. Lightweight Epoxy-Based composites for EMI shielding applications. Journal of Electronic Materials 2020;49:1702–20. https://doi.org/10.1007/s11664-019-07687-5.
[30] Horibe H, Sasaki Y, Oshiro H, Hosokawa Y, Kono A, Takahashi S, et al. Quantification of the solvent evaporation rate during the production of three PVDF crystalline structure types by solvent casting. Polymer Journal 2014;46(2):104–10.
[31] Ruan L, Yao X, Chang Y, Zhou L, Qin G, Zhang X. Properties and applications of the β phase poly(vinylidene fluoride). Polymers (Basel) 2018;10:1–27. https://doi.org/10.3390/polym10030228.
[32] Nazir A. A review of polyvinylidene fluoride (PVDF), polyurethane (PU), and polyaniline (PANI) composites-based materials for electromagnetic interference shielding. Journal of Thermoplastic Composite Materials 2022;35(10):1790–810.
[33] Donley G, Sun Y, Pass G, Adler PH, Beard CE, Owens J, et al. Insect antennae: Coupling blood pressure with cuticle deformation to control movement. Acta Biomaterialia 2022;147:102–19.
[34] Morris SE, Bayram Y, Zhang L, Wang Z, Shtein M, Volakis JL. High-Strength, metalized fibers for conformal load bearing antenna applications. IEEE Transactions on Antennas and Propagation 2011;59:3458–62. https://doi.org/10.1109/TAP.2011.2161442.
[35] Xie Z, Avila R, Huang Y, Rogers JA. Flexible and stretchable antennas for biointegrated electronics. Advanced Materials 2020;32:1902767.
[36] Chakraborty T, Dutta S, Mahapatra AS, Das K, Das S, Roy A, et al. Superior EMI shielding effectiveness of light weight and stretchable x-type hexaferrite-poly

(vinylidene fluoride) laminated nanocomposite materials. Journal of Magnetism and Magnetic Materials 2023;570:170508.
[37] Loke G, Yan W, Khudiyev T, Noel G, Fink Y. Recent progress and perspectives of thermally drawn multimaterial fiber electronics. Advanced Materials 2020;32:1904911.
[38] Faisal NH, Ahmed R, Sellami N, Prathuru A, Njuguna J, Venturi F, et al. Thermal spray coatings for electromagnetic wave absorption and interference shielding: A review and future challenges. Advanced Engineering Materials 2022;24(7).
[39] Pinto GM, Cremonezzi JMO, Ribeiro H, Andrade RJE, Demarquette NR, Fechine GJM. From two-dimensional materials to polymer nanocomposites with emerging multifunctional applications: A critical review. Polymer Composites 2023;44:1438–70.
[40] Wang J, Song Y. Thin films and/or coating for electromagnetic interference and stealth. Inorg Org Thin Film 2021:587–614.
[41] Kumar S, Supriya S, Kar M. Enhancement of dielectric constant in polymer-ceramic nanocomposite for flexible electronics and energy storage applications. Composites Science and Technology 2018;157:48–56. https://doi.org/10.1016/j.compscitech.2018.01.025.
[42] Gan F, Yao Q, Cheng L, Zhang L, Liang Q, Guo J, et al. Fabrication of BaFe12O19/CeO2 composite for highly efficient microwave absorption. Journal of Alloys and Compounds 2022;897:162964.
[43] Widodo RD, Priyono, Rusiyanto, Anis S, Ilham RI, Firmansyah HN, et al. Shrinkage, density and hardness of Hard magnetic material (BaFe12O19) based on iron sand produced by conventional Solid-State reaction process. IOP Conf Ser: Earth Environ Sci 2021;700(1):012001.
[44] Darwish MA, Abosheiasha HF, Morchenko AT, Kostishyn VG, Turchenko VA, Trukhanova EL, et al. Impact of the zr-substitution on phase composition, structure, magnetic, and microwave properties of the BaM hexaferrite. Ceramics International 2021;47(12):16752–61.
[45] Uddin A, Khatoon R, Estevez D, Salem M, Ali A, Attique S, et al. Waste paper cellulose based-MoS2 hybrid composites: towards sustainable green shielding. Materials Today Communications 2022;31:103858.
[46] Briesmeister JF. MCNPTM–A General Monte Carlo N–Particle Transport Code: Manual. n.d.
[47] ALMisned G, Zakaly HMH, Ali FT, Issa SAM, Ene A, Kilic G, et al. A closer look at the efficiency calibration of LaBr 3(Ce) and NaI(Tl) scintillation detectors using MCNPX for various types of nuclear investigations. Heliyon 2022;8(10):e10839.
[48] Zhou W, Cui T, Zhang Z, Yang Y, Yi H, Hou D. Measurement of wide energy range neutrons with a CLYC(Ce) scintillator. Journal of Instrumentation 2023;18(02):P02014.
[49] Şakar E, Özpolat ÖF, Alım B, Sayyed MI, Kurudirek M. Phy-X / PSD: Development of a user friendly online software for calculation of parameters relevant to radiation shielding and dosimetry. Radiation Physics and Chemistry 2020;166:108496. https://doi.org/10.1016/j.radphyschem.2019.108496.
[50] Tekin HO, ALMisned G, Susoy G, Zakaly HMH, Issa SAM, Kilic G, et al. A detailed investigation on highly dense CuZr bulk metallic glasses for shielding purposes. Open Chemistry 2022;20(1):69–80.
[51] Gunoglu K, Varol Özkavak H, Akkurt İ. Evaluation of gamma ray attenuation properties of boron carbide (B4C) doped AISI 316 stainless steel: Experimental, XCOM and Phy-X/PSD database software. Materials Today Communications 2021;29:102793.
[52] Abulyazied DE, Saudi HA, Zakaly HMH, Issa SAM, Henaish AMA. Novel nanocomposites based on polyvinyl alcohol and molybdenum nanoparticles for gamma irradiation shielding. Optics and Laser Technology 2022;156:108560.
[53] Mostafa AMA, Issa SAM, El Agammy EF, Zakaly HMH, Alotaibi BM, Gharghar F. Effect of BaO addition on gamma radiation shielding performance of sodium barium borate glasses using FLUKA code and PhyX/PSD platform. Radiation Physics and Chemistry 2023;206:110766.
[54] Rammah YS, Mahmoud KA, El-Agawany FI, Tashlykov OL, Yousef E. Tm3+ ions-doped phosphate glasses: nuclear shielding competence and elastic moduli. Applied Physics A: Materials Science & Processing 2020;126:1–11. https://doi.org/10.1007/S00339-020-04109-W/FIGURES/9.
[55] Darwish MA, Afifi AI, Abd El-Hameed AS, Abosheiasha HF, Henaish AMA, Salogub D, et al. Can hexaferrite composites be used as a new artificial material for antenna applications? Ceramics International 2021;47(2):2615–23.
[56] Mehdipour M, Shokrollahi H. Comparison of microwave absorption properties of SrFe12O 19, SrFe12O19/NiFe2O4, and NiFe2O4 particles. J Appl Phys 2013;114. https://doi.org/10.1063/1.4816089.
[57] Acharya S, Gopinath CS, Alegaonkar P, Datar S. Enhanced microwave absorption property of reduced graphene oxide (RGO)–Strontium hexaferrite (SF)/Poly (Vinylidene) fluoride (PVDF). Diamond and Related Materials 2018;89:28–34. https://doi.org/10.1016/j.diamond.2018.07.024.
[58] Ben GT, Dhaoui W, Schoenstein F, Talbot P, Mazaleyrat F. Substitution effect of me = al, bi, cr and mn to the microwave properties of polyaniline/BaMeFe11O19for absorbing electromagnetic waves. Journal of Alloys and Compounds 2017;692:774–86. https://doi.org/10.1016/j.jallcom.2016.09.075.
[59] Baji A, Mai Y-W, Li Q, Liu Y. Electrospinning induced ferroelectricity in poly (vinylidene fluoride) fibers. Nanoscale 2011;3:3068–71. https://doi.org/10.1039/C1NR10467E.
[60] Lei T, Yu L, Zheng G, Wang L, Wu D, Sun D. Electrospinning-induced preferred dipole orientation in PVDF fibers. Journal of Materials Science 2015;50:4342–7. https://doi.org/10.1007/s10853-015-8986-0.
[61] Zhong G, Zhang L, Su R, Wang K, Fong H, Zhu L. Understanding polymorphism formation in electrospun fibers of immiscible poly(vinylidene fluoride) blends. Polymer (Guildf) 2011;52:2228–37.
[62] Nguyen TTT, Nguyen HT, Trinh HT, Bui TTT, Le AT, Huy TQ. Effect of the morphological characteristic and composition of electrospun polyvinylidene fluoride/Graphene oxide membrane on its Pb2+ adsorption capacity. Macromolecular Research 2022;30:124–35. https://doi.org/10.1007/s13233-022-0012-1.
[63] El SM, Elkomy GM, Osman H, Nagy MR, El-Sayed F. Structure-electrical conductivity of polyvinylidene fluoride/graphite composites. Journal of Reinforced Plastics and Composites 2012;31:1342–52. https://doi.org/10.1177/0731684412459286.
[64] Ponnamma D, Erturk A, Parangusan H, Deshmukh K, Ahamed MB, Al-Maadeed AA, et al. Stretchable quaternary phasic PVDF-HFP nanocomposite films containing graphene-titania-SrTiO3 for mechanical energy harvesting. Emergent Mater 2018;1:55–65. https://doi.org/10.1007/s42247-018-0007-z.
[65] Shaterian M, Yulchikhani M, Aghasadeghi Z, Hassani AH. Synthesis, characterization, and investigation of electrochemical hydrogen storage capacity in barium hexaferrite nanocomposite. Journal of Alloys and Compounds 2022;915:165350.
[66] Supriya S, Kumar L, Kar M. Optimization of dielectric properties of PVDF–CFO nanocomposites. Polymer Composites 2019;40:1239–50. https://doi.org/10.1002/pc.24840.
[67] Huang J, Cao Y, Shao Q, Peng X, Guo Z. Magnetic nanocarbon adsorbents with enhanced hexavalent chromium removal: Morphology dependence of fibrillar vs particulate structures. Industrial and Engineering Chemistry Research 2017;56:10689–701. https://doi.org/10.1021/acs.iecr.7b02835.
[68] Ponnamma D, Aljarod O, Parangusan H, Ali Al-Maadeed M Al. Electrospun nanofibers of PVDF-HFP composites containing magnetic nickel ferrite for energy harvesting application. Mater Chem Phys 2020;239:122257. https://doi.org/https://doi.org/10.1016/j.matchemphys.2019.122257.
[69] Assar ST, Abosheiasha HF, Mansour D-E-A, Darwish MA. Preparation and investigation of epoxy/Li0.5AlxFe2.5-xO4 nanocomposites for electronic packaging applications. Journal of Alloys and Compounds 2020;821:153533.
[70] Peymanfar R, Keykavous-Amand S, Abadi MM, Yassi Y. A novel approach toward reducing energy consumption and promoting electromagnetic interference shielding efficiency in the buildings using brick/polyaniline nanocomposite. Construction and Building Materials 2020;263:120042. https://doi.org/10.1016/j.conbuildmat.2020.120042.
[71] Qin M, Zhang L, Wu H. Dielectric loss mechanism in electromagnetic wave absorbing materials. Advancement of Science 2022;9:1–24. https://doi.org/10.1002/advs.202105553.
[72] Liu J, Zhang L, Zang D, Wu H. A competitive reaction strategy toward binary metal sulfides for tailoring electromagnetic wave absorption. Advanced Functional Materials 2021;31:2105018.
[73] Sikiru S. Ionic transport and influence of electromagnetic field interaction within electric double layer in reservoir sandstone. Journal of Molecular Liquids 2021;344:117675.
[74] Xia L, Feng Y, Zhao B. Intrinsic mechanism and multiphysics analysis of electromagnetic wave absorbing materials: New horizons and breakthrough. Journal of Materials Science and Technology 2022;130:136–56.
[75] Wang L, Guan Y, Qiu Xu, Zhu H, Pan S, Yu M, et al. Efficient ferrite/Co/porous carbon microwave absorbing material based on ferrite@metal–organic framework. Chemical Engineering Journal 2017;326:945–55.
[76] Acharya S, Alegaonkar P, Datar S. Effect of formation of heterostructure of SrAl4Fe8O19/RGO/PVDF on the microwave absorption properties of the composite. Chemical Engineering Journal 2019;374:144–54. https://doi.org/10.1016/j.cej.2019.05.078.
[77] Shu R, Zhang J, Guo C, Wu Y, Wan Z, Shi J, et al. Facile synthesis of nitrogen-doped reduced graphene oxide/nickel-zinc ferrite composites as high-performance microwave absorbers in the x-band. Chemical Engineering Journal 2020;384:123266.
[78] Darwish MA, Turchenko VA, Morchenko AT, Kostishyn VG, Timofeev AV, Sayyed MI, et al. Heterovalent substituted BaFe12-xSnxO19 (0.1≤ x ≤1.2) m-type hexaferrite: Chemical composition, phase separation, magnetic properties and electrodynamics features. Journal of Alloys and Compounds 2022;896:163117.
[79] Fu XY, Zheng Q, Li L, Cao MS. Vertically implanting MoSe2 nanosheets on the RGO sheets towards excellent multi-band microwave absorption. Carbon N Y 2022;197:324–33. https://doi.org/10.1016/j.carbon.2022.06.037.
[80] Han M, Zhou M, Wu Y, Zhao Y, Cao J, Tang S, et al. Constructing angular conical FeSiAl/SiO2 composites with corrosion resistance for ultra-broadband microwave absorption. Journal of Alloys and Compounds 2022;902:163792.
[81] Wu Y, Zhao Y, Zhou M, Tan S, Peymanfar R, Aslibeiki B, et al. Ultrabroad microwave absorption ability and infrared stealth property of Nano-Micro CuS@rGO lightweight aerogels. Nano-Micro Lett 2022;14:1–17. https://doi.org/10.1007/s40820-022-00906-5.
[82] Li X, Xu D, Zhou Di, Pang S, Du C, Darwish MA, et al. Magnetic array vertically anchored on flexible carbon cloth with “magical angle” for the increased effective absorption bandwidth and improved reflection loss simultaneously. Carbon N Y 2023;210:118046.
[83] Abouhaswa AS, Zakaly HMH, Issa SAM, Pyshkina M, El-Mallawany R, Mostafa MYA. Lead borate glasses and synergistic impact of lanthanum oxide additive: optical and nuclear radiation shielding behaviors. Journal of Materials Science: Materials in Electronics 2020;31:14494–501. https://doi.org/10.1007/s10854-020-04009-y.
[84] Zakaly HMH, Issa SAM, Tekin HO, Badawi A, Saudi HA, Henaish AMA, et al. An experimental evaluation of CdO/PbO-B2O3 glasses containing neodymium oxide:

Structure, electrical conductivity, and gamma-ray resistance. Materials Research Bulletin 2022;151:111828.
[85] Bashter II. Calculation of radiation attenuation coefficients for shielding concretes. Annals of Nuclear Energy 1997;24:1389–401. https://doi.org/10.1016/S0306-4549(97)00003-0.
[86] Alzahrani JS, Yilmaz E, Çalişkan F, Alrowaili ZA, Olarinoye IO, Alqahtani MS, et al. Synthesis and optimization of B2O3-based glass: Influence of MgO on hardness, structure properties, and radiation shielding performance. Materials Today Communications 2023;37:106933.